Diffusion MRI Anisotropy in the Cerebral Cortex is Determined by Unmyelinated Tissue Features

Colin Reveley[1,2,*], Frank Q Ye[3], Rogier B Mars[1,4], David A Leopold[3,5]

[1] Wellcome Centre for Integrative Neuroimaging, Centre for fMRI of the Brain (FMRIB), Nuffield Department of Clinical Neurosciences, John Radcliffe Hospital, University of Oxford, Headington, Oxford, OX9 3DU, UK.

[2] Department of Informatics, University of Sussex, Falmer, Brighton BN1 9QJ, UK

[3] Neurophysiology Imaging Facility, National Institute of Mental Health, National Institute of Neurological Disorders and Stroke, National Eye Institute, National Institutes of Health, Bethesda, MD

[4] Donders Institute for Brain, Cognition and Behaviour, Radboud University Nijmegen, Nijmegen, The Netherlands.

[5] Section on Cognitive Neurophysiology and Imaging, Laboratory of Neuropsychology, National Institute of Mental Health, National Institutes of Health, Bethesda, MD

*correspondence: reveley@gmail.com

Abstract

The diffusion of water molecules through the brain is constrained by tissue and cellular substructure, which imposes an anisotropy that can be measured through diffusion magnetic resonance imaging (dMRI). In the white matter, myelinated axons strongly shape diffusion anisotropy; however, in gray matter the determinants of dMRI signals remain poorly understood. Here we investigated the histological tissue properties underlying dMRI anisotropy and diffusivity in the cerebral cortex of the marmoset monkey. We acquired whole brain ex vivo dMRI data designed for high signal-to-noise at ultra-high (150μm) resolution. We compared the MRI to myelin- and Nissl-stained histological sections obtained from the scanned brain. We found that dMRI anisotropy corresponds most strongly not with cortical myelin content, but rather with the microscale anisotropy of tissue features, most notably those unmyelinated features highlighted by Nissl staining. The results suggest that dMRI anisotropy in gray matter derives from the organization of unmyelinated neurites, which are known to be affected by neurodegenerative diseases.

Introduction

Recent advances in high resolution diffusion MRI (dMRI) methods have revealed significant diffusion anisotropy in the cerebral cortex gray matter[1–7]. This finding provides an opportunity to extend the use of dMRI beyond its well-established application for characterizing white matter projections. Determining the cellular and histological features that give rise to this anisotropy is important, because this could offer a way for MRI methods to detect and measure the detailed cytoarchitectural properties of gray matter, both in healthy tissue and in disease states. Cytoarchitecturally grounded MRI contrasts might link foundational histological studies in the medical field[8] to *in vivo* studies in humans at the level of individual subjects, and could aid in the detection of neuropathology. For example, linking dMRI variation to tissue structure could be applied to track the progression of cortical pathology during the early stages of Alzheimer's disease[9], or to track tissue changes in conditions like PTSD[10].

The histological basis of diffusion anisotropy in gray matter is not yet well explored[11]. Based on principles derived from the analysis of white matter, where the majority of previous histological comparisons have been carried out[12,13], it seems likely that both the density and arrangement of myelinated fibers contribute to cortical dMRI patterns[2,14–20]. Large caliber myelinated axons are one component of gray matter, which for example include extrinsic projections emanating from layer II/III into white matter[21,22], and afferent axons projecting into cortex. Other myelinated axons in gray matter, however, differ from those in the white matter, being less densely packed, having a much smaller caliber, or having matted structure rather than forming coherent bundles[23].

The spatial distribution of cortical myelin density varies substantially by horizontal location (anatomical region) and by vertical (laminar) position. The myelin content of voxels may be assessed using a wide variety of MRI contrasts[12,13,24] for example the T1w/T2w or magnetization transfer ratio (MTR). Such assessments are the principal means by which anatomical regions of the gray matter are identified in-vivo at present[25]. Quantitative validation of these contrasts in both white and gray matter is ongoing, but they tend to show more reliable correlations to histologically measured myelin content than do measures of dMRI anisotropy or diffusivity[12,13,24]. There is good evidence[3,26] that the organization, rather than the density, of myelinated fibers drives dMRI anisotropy in a way that is not reflected in contrasts like T1w or MTR, although this has not yet been demonstrated quantitatively[2].

76 There are significant variations in myelinated axon organization between cortical anatomical regions[23,27]
77 and these differences may be reflected in diffusion anisotropy.

78 However, in contrast to white matter, the microstructure of gray matter is dominated by non-
79 myelinated substructures and so it is possible that these shape the diffusion signal more than
80 myelinated axons[28,29], or do so in a different way[30]. Previous work in the field of dMRI indicates that lipid
81 cell membranes are more important determinants of diffusion anisotropy than myelin per se[30]. In white
82 matter, these elements covary because the overwhelming majority of neurites are myelinated axons, so
83 the distinction between myelinated and non-myelinated neurites has not been of great importance[31].
84 This distinction may be much more important in gray matter, and some qualitative evidence[2,3,32]
85 suggests that non-myelinated tissue components could be linked to dMRI anisotropy.

86 At a more detailed level, previous dMRI studies have found that the dominant direction of diffusion
87 anisotropy in the cortex is nearly always perpendicular (henceforth, "vertical") to the pial surface, with
88 the exception of thin zones directly adjacent to the pial and white matter boundaries[3,33–35]. Just as the
89 diffusion orientations in white matter reflect the organization of axonal projections into directed
90 bundles, the pronounced vertical bias in gray matter diffusion orientations may reflect the organization
91 of cell bodies, axons, dendrites and other tissue components into columnar structures[2,3]. Vertically
92 oriented structures in gray matter include some myelinated axons[21,22], but they also include, for
93 example, apical dendrite bundles projecting vertically from deep to superficial layers[3,32,36,37], as well as
94 the neurites of many other more regional and layer specific cell types[22,36,38].

95 In this study we investigate the extent to which measures computed from histological stains for
96 myelinated fibers and Nissl bodies reflect dMRI anisotropy and diffusivity in the gray matter. In
97 comparison to white matter, gray matter exhibits significant variation in myelin density and other
98 material composition within small areas of space. We therefore emphasize high SNR and high spatial
99 resolution in our dMRI acquisition, and spatially precise co-registration in our analysis. We use the
100 foundational diffusion tensor model of the dMRI signal[39] due to its mathematical simplicity, its minimal
101 assumptions about tissue composition and its conceptual similarity to the structure tensor model of
102 histological image anisotropy[40]. We report that dMRI fractional anisotropy (dMRI-FA) in the marmoset
103 cerebral cortex best matches histological anisotropy (HA), rather than myelin content. Myelin content
104 has a comparatively poor correspondence with dMRI-FA, and is much better reflected in a different MRI
105 measure, namely the magnetization transfer ratio (MTR). We then show that the anisotropy of Nissl-

106 stained tissue (Nissl-HA) has the strongest correspondence with MRI diffusion, including dMRI-FA as well
107 as its underlying diffusivity components. Together, the findings suggest that dMRI-FA in the cerebral
108 cortex gray matter is determined principally by unmyelinated components of the tissue, such as
109 dendrites, glial processes and unmyelinated axons.

110 Results

111 To assess which histological features of the gray matter best matched the spatial variation of dMRI-
112 FA, we compared the dMRI data to histological sections from the same brain. Analysis focused on the
113 brain of a marmoset (case P) that was first scanned *ex vivo* using high resolution and signal-to-noise MRI
114 and then sectioned and stained for histological analysis.

115 The brain was scanned for 58 hours on a 7-T Bruker preclinical scanner with 450mT/m gradient
116 coils. Six whole-brain volumes at 150μm isotropic resolution were averaged for each of 60 diffusion
117 encoded directions and two B0 volumes. This extensive averaging resulted in a dMRI dataset with a
118 signal-to-noise ratio of approximately 85 in gray matter. In addition, magnetization transfer ratio (MTR)
119 volumes were acquired in a separate session from the same brain at an isotropic spatial resolution of
120 75μm. The MTR sequence is known to be sensitive to myelin content[41]. The dMRI volumes were
121 resampled to the higher MTR resolution for analysis using a spline interpolation.

122 After MRI scanning, the brain's left and right hemispheres were sectioned into coronal and sagittal
123 sections, respectively, at 50μm on a freezing microtome. Adjacent sections were stained for Nissl
124 bodies using the Thionin stain, and for myelin using the Gallyas silver stain. For quantitative analysis,
125 nine strips of gray matter in the dorsal frontal and parietal lobes were chosen for this comparison based
126 on their low curvature, since cortical curvature can affect dMRI-FA values[42]. Non-linear registration

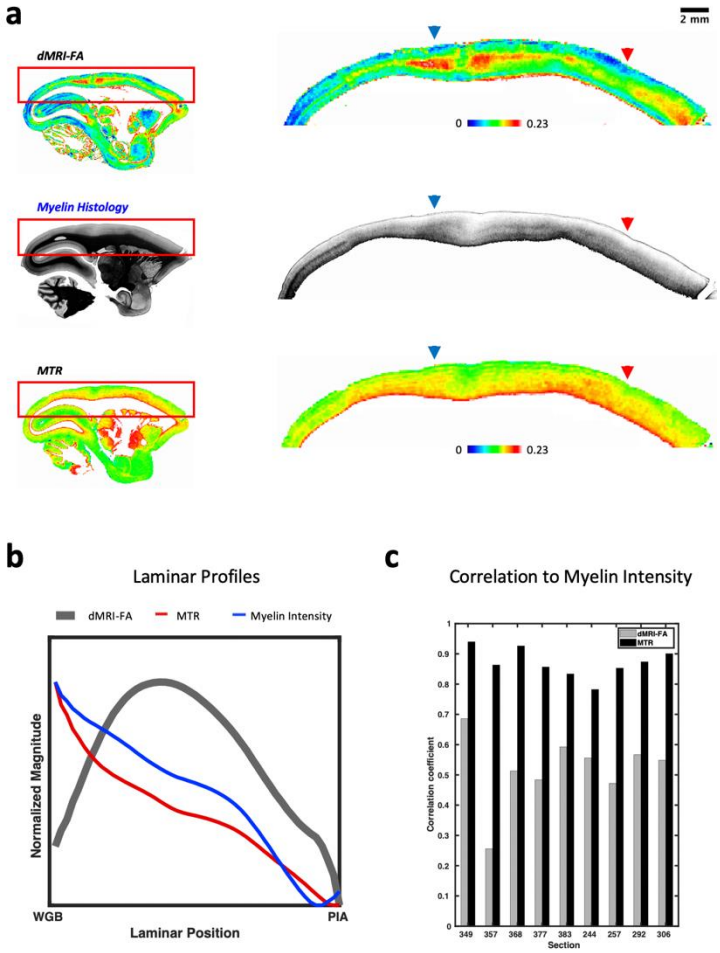

Figure 1. Comparison of dMRI FA to corresponding myelin histology and MTR MRI data obtained from the same tissue in the right hemisphere of marmoset monkey case P. ***a)*** *Sagittal sections of dMRI-FA (**top**), Myelin histology (**center**) and MTR MRI (**bottom**). The spatial variation of dMRI-FA in vertical (laminar) and horizontal direction showed minimal correspondence with the pattern of myelin intensity, but the variation of the MTR MRI closely mirrored the myelin variation. In some regions of high myelination, the dMRI-FA was high (red arrow) whereas in others it was low (blue arrow).* ***b)*** *Normalized average laminar profiles of FA, MTR and myelin intensity through the cortical thickness in the brain's left hemisphere, derived from cortical parcellation (see **Methods, Figure 3**).* ***c)*** *Histogram of correlation coefficients between MRI variables and histological myelin intensity over the nine sections of coronal histology used in this study. MTR MRI shows much higher correspondence with myelin intensity than dMRI-FA does.*

allowed for a direct and precise pixel to pixel comparison of diffusion and histological parameters at 150μm spatial scale (see **Methods**, **SI Figure 1**).

dMRI fractional anisotropy does not reflect myelin content

We began our analysis with a simple pixelwise correlation of MRI and histology within the nine registered sections. Our first question was whether the patterns of dMRI-FA matched the distribution of myelin intensity, as might be expected based on some previous studies in white matter regions[12,13]. We

133 found spatial variation of dMRI-FA was a poor match for the myelin intensity measured through
134 histological staining. This difference was evident both across laminae (henceforth, *vertically*) and along
135 the cortical sheet (henceforth, *horizontally*), as illustrated in a sagittal example section in **Figure 1a**.
136 Comparing the dMRI-FA to the myelin stain intensity, there are areas in which they appear to match
137 (blue arrow) and others in which they clearly do not (red arrow). In the vertical direction, myelin
138 intensity declines monotonically from the white matter to the pia[43]. dMRI-FA behaves differently, being
139 strongest in the middle cortical layers, and lowest near the white matter and pial boundaries (**Figure**
140 **1b**)[4,44]. This example also shows that, in contrast to dMRI-FA, the MTR MRI contrast closely matches the
141 laminar pattern of myelin staining, following from the known sensitivity of the MTR MRI sequence to
142 large macromolecules[41]. Across all sections, the correspondence of the myelin intensity was much
143 higher to the MTR MRI contrast than to the dMRI-FA contrast (**Figure 1c**).

144 *Fractional anisotropy of dMRI matches that of histology*

145 Having established that myelin stain intensity is only modestly correlated to dMRI-FA, we next
146 turned our attention to a comparison of dMRI parameters with tissue organization as reflected in the
147 cell body and myelin histology. In each voxel, the diffusion tensor provides a principal orientation, and
148 scalar indices of anisotropy such as dMRI-FA. For direct comparison, we sought to generate parameter
149 maps from the histology at the same spatial resolution and with equivalent information as the dMRI. To
150 achieve this, we computed the structure tensor (ST) of the cell body and myelinated fiber histology at
151 microscopic scale, weighted over a mesoscopic spatial area that matched the dMRI acquisition
152 resolution of 150μm (see **Methods**). We then resampled the resulting parameter maps to the MRI
153 display resolution of 75μm (**Figure 2**). Like the diffusion tensor, the structure tensor provides both
154 vector and scalar data, in the form of mean orientations and ST coherence[45]. For both the myelin- and
155 Nissl-based sections, the principal ST orientation was strikingly uniform and nearly always perpendicular
156 to the pial surface (i.e. vertical) closely matching the orientation map obtained from the dMRI diffusion
157 tensor (**Figure 2a**). While it was not the focus of the present study, we also found that the tractography
158 computed from the histological and dMRI data yielded qualitatively nearly identical results (**SI Figure 3**).
159 Only in thin laminar zones directly adjacent to the pia and the white matter did this principal orientation
160 deviate significantly from the vertical and differ across measurements.

161

ST coherence is similar to dMRI-FA in that it reflects the degree of alignment of objects. However, unlike dMRI-FA[2,15], ST coherence does not reflect object density[45] within that area. We therefore created measures of histological anisotropy (Nissl-HA and myelin-HA) by adjusting the histological ST coherence values to incorporate a pixelwise approximation of neurite density. To derive myelin-HA, we used the product of normalized histological myelin density and myelin ST coherence. For Nissl data we used the product of Nissl ST coherence and the Nissl derived "neurite fraction"[46] (see **Methods**). These measures served as summary statistics whose variation could be compared systematically with that of the dMRI-

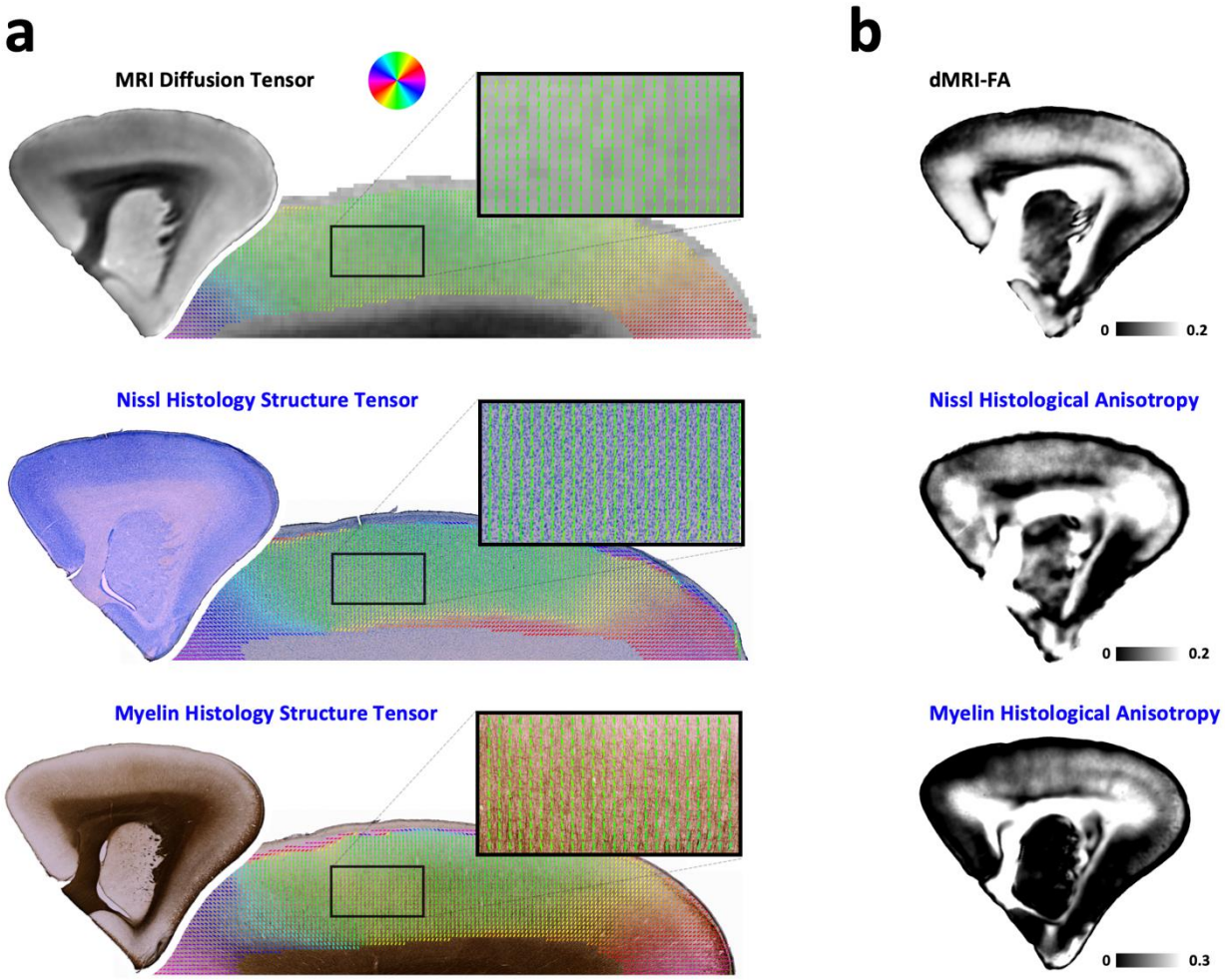

*Figure 2. Properties of directional MRI and histology data. For comparison with MRI data, the weighted structure tensor of the myelin and Nissl histology images was computed over a 150μm area (see **Methods**). **a**) Orientation data derived from Nissl and myelin histology and from dMRI are similar, showing columnar, vertically oriented vectors. The overall pattern of orientations in the gray matter is remarkably similar for the data computed from histology and from dMRI. **b**) The right column shows dMRI-FA and non-linearly registered histology anisotropy maps which show the degree of edge dispersion from the mean in 75μm tiles (see **Methods**).*

FA across the gray matter (**Figure 2b**). While the inclusion of neurite density into the HA measure was deemed appropriate for this comparison, qualitatively similar results for all figures were obtained using maps of the histological coherence alone (**SI Figure 2**).

For each section, we quantitatively compared the spatial variation of dMRI-FA to the Nissl-HA, myelin-HA, and myelin stain intensity scalar parameter maps (see **Methods**). For completeness, we also compared the MTR MRI data to the same histological parameters. To accommodate anatomical variety and potential inconsistencies in histological stain intensity, we employed a parcellation approach in our analysis of the gray matter. In each of the nine low-curvature sections, we compared the spatial variation in the MRI and histological parameter maps by computing the correlation over multiple parcellated subdivisions spanning the thickness of the cortex (example red trapezoids in **Fig. 3**, see **Methods, SI Figure 4**). We focused analysis on a horizontal parcellation width of 300 μm, though the results of the analysis were robust to parcel sizes ranging over a hundred-fold in area (see **SI Figure 5**). Within a given parcel, a pixel-by-pixel correlation of variation within each column revealed different levels of correspondence for the different histological and MRI parameters. This difference can be seen in the example parcel in **Figure 3 (bottom row),** the strongest spatial correspondence with the dMRI-FA measure was the anisotropy in the Nissl-stained sections, Nissl-HA, while the strongest correspondence with the MTR was the myelin intensity.

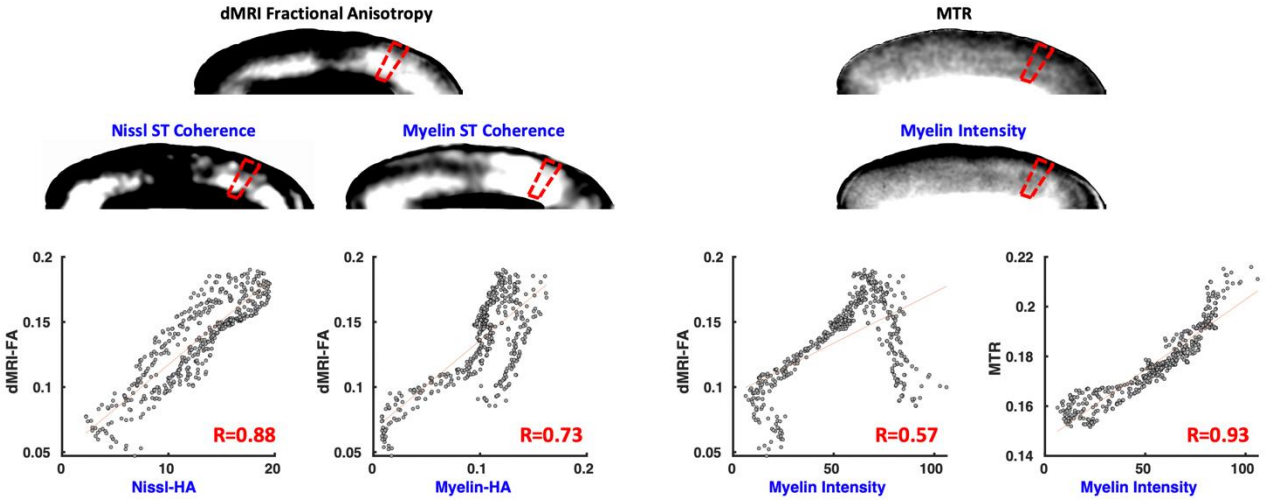

Figure 3. Example correlation of Histology and MRI variables sampled in columnar parcels. Top row: non-linearly co-registered histology parameter maps and MRI at 75μm resolution. The red trapezoids indicate a columnar parcel example. Bottom row shows representative scatter plots and Pearson correlation coefficients between histological variables and MRI variables.

We evaluated such correlations across all 393 parcels in the nine sections for the different MRI and histological parameter maps (**Figure 4a**). Across the cortex, the strongest correlation with dMRI-FA was found in the Nissl histological anisotropy (Nissl-HA) (median 0.76, mean 0.72). Significantly less correlated were the myelin anisotropy (myelin-HA, median 0.63, mean 0.57) and myelin intensity (MI, median 0.47, mean 0.39). Nissl-HA and myelin-HA were also correlated moderately to one another (median 0.60, mean 0.55) (**SI Figure 6**). The difference in correlation profile between Nissl-HA and myelin-HA was even more pronounced using a measure of in-plane dMRI anisotropy[40] in place of dMRI-FA (**SI Figure 7**), yielding correlations with Nissl-HA (median 0.77, mean 0.74), myelin-HA (median 0.64, mean 0.56) myelin (median 0.43, mean 0.37) with a smaller interquartile range for Nissl-HA and larger for myelin-HA. For comparison, the MTR MRI contrast had a very strong spatial covariation with the myelin intensity (**Figure 4b**, median 0.94, mean 0.93).

The shared variation of dMRI-FA with Nissl-HA suggests that the cortical dMRI-FA is strongly shaped by unmyelinated components such as cell bodies, dendrites and unmyelinated axons. Its much weaker

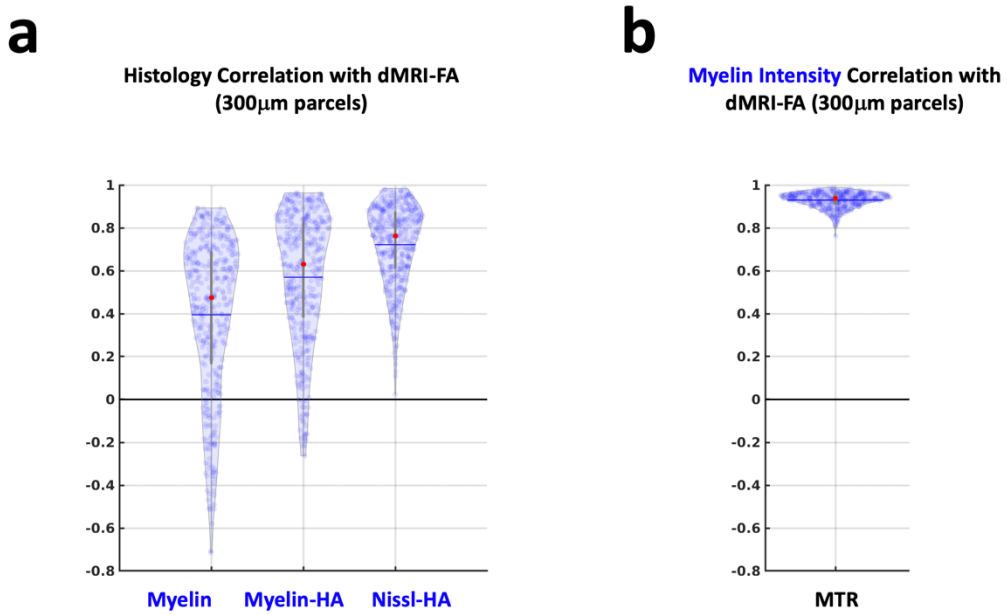

*Figure 4. The distribution of correlation coefficients between histological parameters and dMRI-FA over all 393 parcels of cortex. Each point in the distribution is the Pearson correlation between the variables sampled in a vertical parcel (see **Methods**). Red dot shows median value, blue line shows mean and vertical gray bars show lower and upper quartiles. **a)** Correlation of Histological variables to dMRI-FA **b)** Correlation of MTR to myelin intensity.*

relationship to the myelin-stained sections, and particularly to the myelin intensity distribution, suggests that myelinated axons may have a relatively minor contribution to dMRI anisotropy in the cerebral cortex.

203 *Laminar and tangential variation in anisotropy*

204 Given that the laminar (vertical) and tangential (horizontal) dimensions of the cortex differ substantially
205 in their architectural variation, we performed additional analyses to consider these dimensions

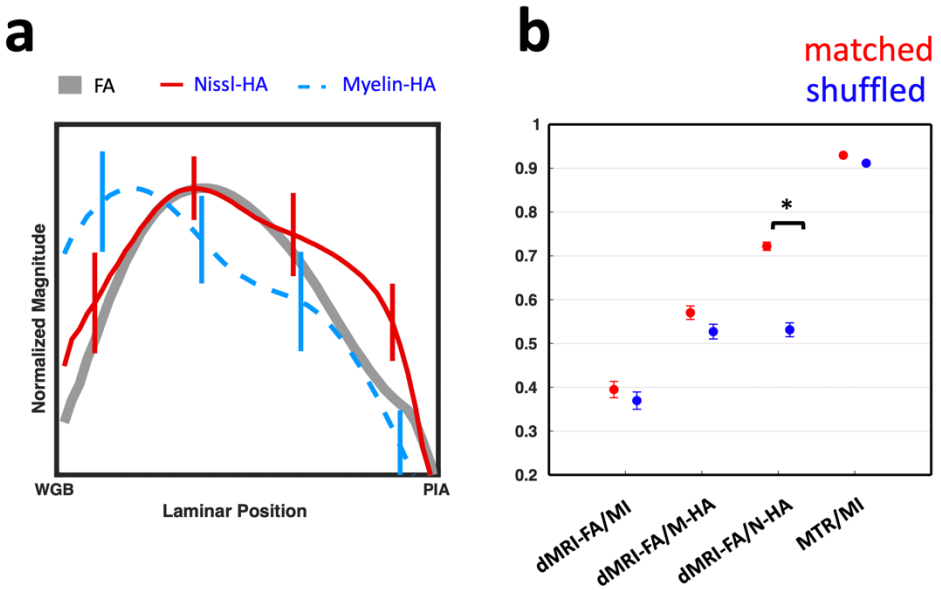

Figure 5. Average laminar profiles of FA, Nissl-HA and myelin-HA across all parcels, and the results of a spatial randomization condition to test the regional specificity of parcel-wise histology to MRI correlations. The results show Nissl-HA more closely matches the laminar profile of dMRI-FA, and is more sensitive to shuffling of horizontal MRI locations ***a)*** *Normalized laminar profiles of dMRI-FA, Myelin-HA and Nissl-HA through the cortical thickness, computed from the average of all columnar parcels (see* ***Methods****). WGB indicates the white/gray matter boundary, PIA indicates the pial surface (see* ***Methods, Figure 3****)* ***b)*** *The change in mean correlation coefficient when the cortical parcels of the histology parameters and those of the dMRI-FA are shuffled between random horizontal locations. Bars indicate standard error. The star indicates significance under a paired t-test.*

206 separately. First, we analyzed the mean laminar variation of the dMRI-FA and compared it to the
207 histological anisotropy (**Figure 5a**). Collapsing the data across all horizontal cortical positions (see
208 **Methods**) revealed a pronounced laminar profile for each of the measured parameters. The dMRI-FA
209 profile had its highest responses in the middle or lower-middle cortical layers, with a decline in
210 anisotropy in both upper layers near the pia, and lower layers near the white gray boundary (WGB). This
211 profile was consistent with results from human dMRI[4], although our higher resolution data revealed
212 significantly more underlying variation in the laminar profiles of individual horizontal locations (**SI Figure**
213 **8, SI Figure 9**). The average laminar profile across horizontal regions in **Figure 5a** resembled the
214 observed histological anisotropy, with somewhat stronger correspondence to the Nissl-HA measure. As
215 described earlier, the profile of dMRI-FA differed markedly from the more monotonic profiles of myelin

intensity and MTR (**Figure 1c**). The average laminar Nissl-staining intensity exhibited nearly the inverse profile to the myelin intensity, having its highest intensity in the superficial layers (**SI Figure 10**).

Given these conspicuous laminar profiles, we next asked to what extent the observed correspondence between dMRI-FA and the two measures of histological anisotropy could be ascribed to laminar variation alone. To address this question, we performed an analysis in which we shuffled the horizontal locations of the columnar parcels in the histological parameter maps relative to the dMRI-FA maps. If such shuffling were to have no effect on the observed correlation, then we could conclude that the parcel correlation results in **Figure 4** are fully explained by laminar variation that follows a stereotypical pattern across the data. We found that shuffling strongly affected the correlation of the Nissl-HA with the dMRI-FA but, had no significant effect on the other histological/MRI correlations (**Figure 5b**). For the Nissl-HA, tangential (horizontal) shuffling causing the mean correlation to drop significantly, from 0.72 to 0.52 (t-test, $p<10^{-10}$). These results indicate that, while the average laminar profile (**Figure 5a**) generally determines the correspondence of dMRI with myelin-HA and myelin intensity, the Nissl-HA measure was unique matching the horizontal variation of dMRI-FA.

Histological correlation with dMRI diffusivity components

We next investigated relationships between histological anisotropies (Nissl-HA, myelin-HA) and the specific directional diffusivities that underlie diffusion anisotropy in gray matter. dMRI-FA is a composite measure that relates to the ratio of axial and radial diffusivities. Axial diffusivity (AD), $\lambda_{\parallel} \equiv \lambda_1 > \lambda_2, \lambda_3$, describes the mean rate of diffusion along the principal diffusion tensor axis. As described earlier (**Figure 2a**), in gray matter the principal tensor axis for both dMRI and histology is overwhelmingly oriented in the vertical direction. Radial diffusivity (RD), $\lambda_{\perp} \equiv (\lambda_2 + \lambda_3)/2$, refers instead to diffusion perpendicular to the principal axis, in the horizontal direction in the gray matter.

Applying the same strategy as above in **Figure 4**, we computed the parcel-wise spatial correlation of MRI diffusivity parameters AD and RD with that of dMRI-FA (**Figure 6a**). We also computed the spatial correlation of AD and RD with the two measures of histological anisotropy (**Figure 6b**). We found that the diffusivity correlation profile of Nissl-HA was qualitatively similar to that dMRI-FA, whereas that of myelin-FA was not. Specifically, of the two histological measures, only Nissl-HA exhibited any positive correlation to AD. We also noted that myelin-HA exhibited a very strong anti-correlation to RD, and we

244 found that laminar variation in myelin-HA closely matched laminar variation in RD (**SI Figure 11**). MTR
245 and myelin intensity both show a strong anti-correlation to RD (**SI Figure 12**). dMRI-FA in gray matter

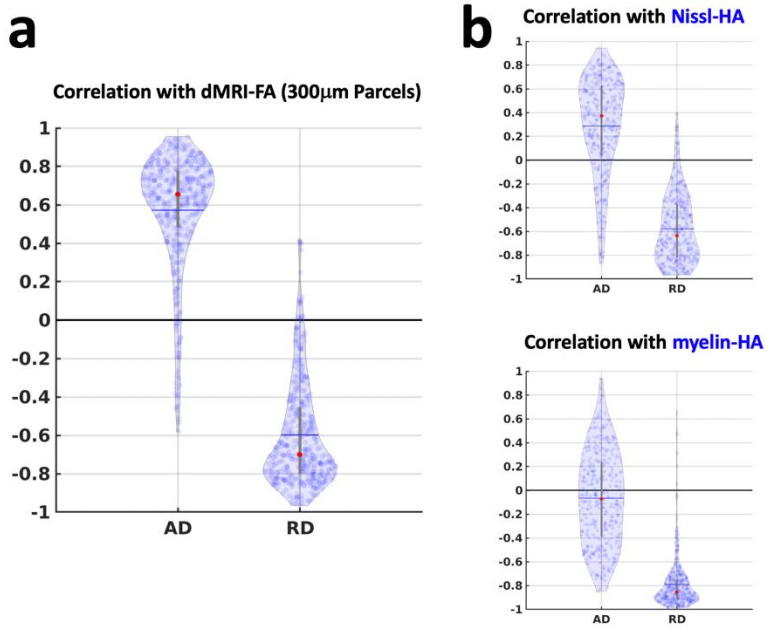

Figure 6. Distribution of correlation coefficients between histological and dMRI anisotropy on one hand and directional diffusivities on the other. Nissl-HA exhibits a profile that is more similar to dMRI-FA than that of myelin-HA. ***a)*** *dMRI-FA correlates to increases vertical diffusivity (AD) and decreases in horizontal diffusivity (RD).* ***Top Right*** *Nissl histological anisotropy (Nissl-HA) exhibits modest positive correlation to AD and negative correlation to RD, indicating that Nissl-HA and dMRI are associated with a similar mechanism of diffusion anisotropy.* ***Bottom Right*** *myelin histological anisotropy exhibits no mean correlation to vertical diffusivity and very strong correlation to horizontal diffusivity, as predicted from previous studies* [18]

246 appears to be caused both by increases in axial diffusivity and decreases in radial diffusivity relative to
247 the isotropic case. Spatial variation in these diffusivity parameters are similarly reflected in Nissl-HA
248 parameter, while myelin-HA and myelin intensity appear primarily to affect only RD.

249 *The exception of granular layer 4*

250 While the Nissl-HA was generally a reliable marker for dMRI-FA variation across gray matter voxels,
251 there was a notable exception. In layer 4 of granular regions of the cortex, the Nissl-HA and dMRI-FA did
252 not match as expected, since the Nissl-HA was low but the dMRI-FA was high, driven by elevated axial
253 diffusivity (**Figure 7a**, green). While above we interpreted Nissl-HA to be an indicator of oriented
254 neurites, this assumption likely does not hold true in layer 4, where the Nissl-staining is dominated by
255 round and unoriented, granular neurons (see **SI Figure 13**), and there is a pronounced gap in

myelination (**Figure 7b**). While most cortical neurons outside of layer 4 are pyramidal in shape[47], both excitatory and inhibitory layer 4 cells have a stellate morphology with rounded cell bodies. While these cell bodies are unlikely to elevate dMRI-FA, it is known that they project highly branched, vertically oriented, unmyelinated axons[48]. Furthermore, layer 4 is a site where many thalamic afferents lose their myelin sheath and branch heavily, including into vertically oriented collaterals (**Figure 7b**, right)[49]. Taken

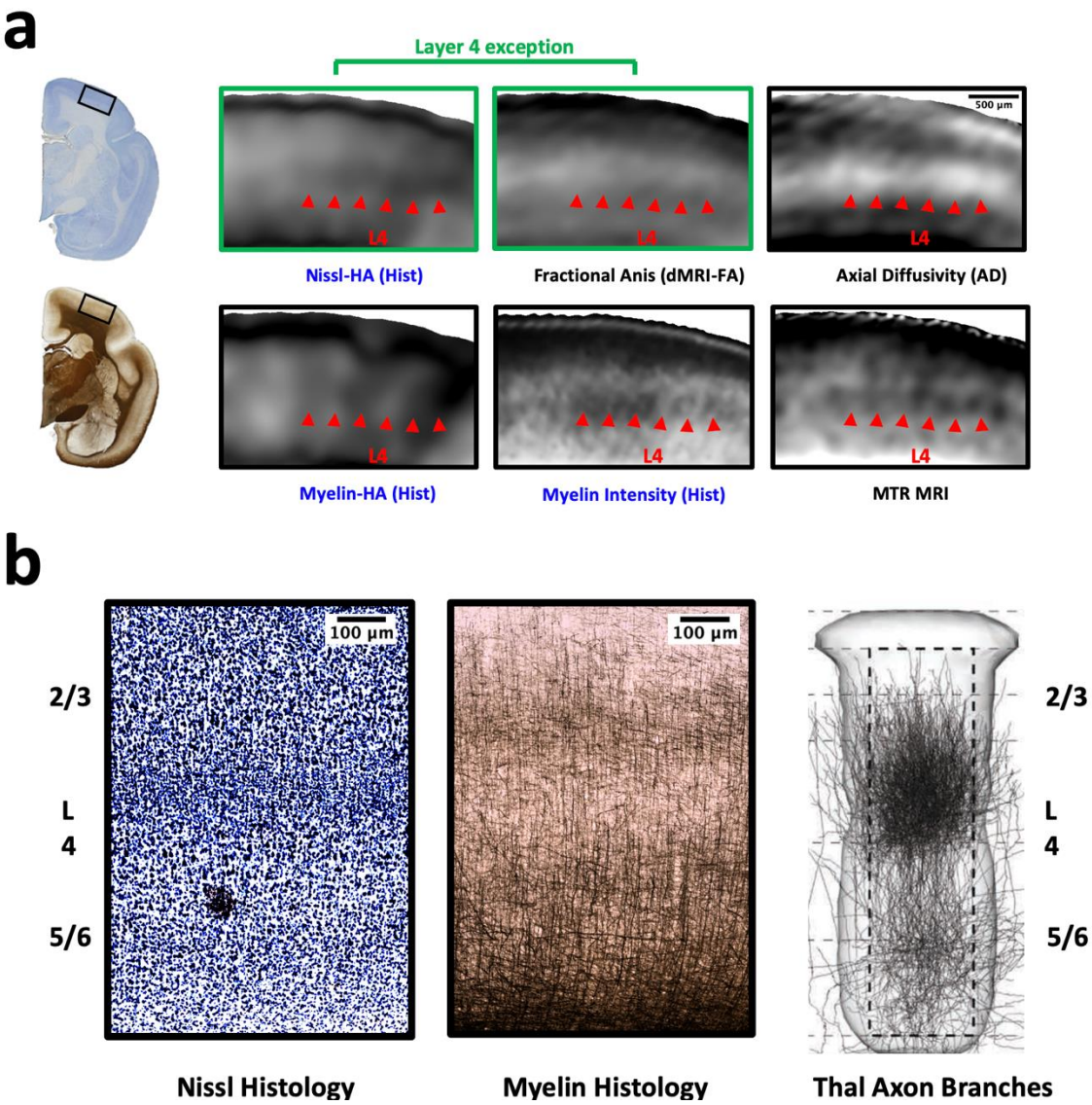

Figure 7. In granular cortex, layer 4 is identifiable in Nissl histology by many small cell bodies and in myelin histology by a local decrease in stain intensity. In dMRI data layer 4 is associated with a local increase in Axial diffusivity (AD) and in MTR data by a band of low intensity. ***a)*** *dMRI, MTR and histologically derived contrasts.* ***B) Left*** *Illustrative detail of the Nissl histology from an ROI of granular cortex. The internal granule layer is visible as a band of small, round cells.* ***Middle*** *the same region in myelin histology exhibits a gap in myelination. CLAHE contrast enhancement was applied uniformly across both myelin and Nissl images for display* ***Right*** *The highly branched, unmyelinated layer 4 terminals of axons from 8 thalamic afferent cells in rat Barrel cortex, reproduced from[49].*

261 together, the elevated MRI axial diffusivity in granular layer 4 may be thus hypothesized to result from
262 these and other unmyelinated axons, which cannot be observed in either the Nissl or myelin-stained
263 sections.

264 Discussion

265 The results of this study suggest that diffusion MRI in cortical gray matter can capture important,
266 hitherto inaccessible cytoarchitectural tissue properties in vivo. We analyzed the basis of dMRI-FA in the
267 cerebral cortex gray matter of the marmoset monkey, scanned at very high signal-to-noise and spatial
268 resolution. We focused on the diffusion tensor as a straightforward and well understood model of
269 diffusion with minimal prior assumptions about tissue properties[50]. We systematically compared dMRI-
270 FA to finely co-registered histological parameter maps obtained from the same brain. To accommodate
271 anatomical variety and potential inconsistencies in histological stain intensity, we used a cortical
272 parcellation approach to conduct a mesoscale analysis of gray matter histological features that link to
273 the spatial variation in dMRI properties. For comparison we also analyzed an MTR MRI data set, which is
274 sensitive to large macromolecules such as myelin[41].

275 Our principal finding was that fractional anisotropy correlated strongly with histological anisotropy
276 derived from the structure tensor, and much less so with histological myelin density. However, myelin
277 density did correlate very strongly with the MTR MRI contrast obtained from the same brain. We found
278 that the dMRI-FA was particularly strongly correlated with the Nissl histological anisotropy, a result that
279 identifies unmyelinated neurites as the principal determinant of dMRI-FA. Our second main finding was
280 that Nissl-HA and myelin-HA correlated differently to the diffusivity components of dMRI-FA. Like dMRI-
281 FA, Nissl-HA positively correlated to axial diffusivity - but myelin-HA did not. These two distinct
282 correlation profiles indicate that myelinated and non-myelinated neurites in gray matter have
283 qualitatively different contributions to diffusion anisotropy. An exception to the general pattern was
284 found in granular layer 4, where high dMRI-FA and high axial diffusivity were not accompanied by
285 elevated Nissl-HA or myelin-HA. We hypothesize that this exception stems from unmyelinated axons
286 and other neurites known to penetrate that layer in great numbers[49], but which are undetectable with
287 either Nissl or myelin staining.

288 The finding that the cell body anisotropy (Nissl-HA) had the strongest correlation to dMRI-FA was
289 somewhat unexpected. This association is probably not due to the properties of cell bodies

290 themselves[2,3,7,32]; however, the arrangement of cell bodies in Nissl data may be a reliable marker for the
291 arrangement of neurites and glial processes[22,38,51,52], and this has previously been used to detect and
292 quantify the columnar neurite architecture of the cortex[51]. The relative area of the unstained portion of
293 Nissl stained sections has previously been used to quantify the neuropil fraction, including non-
294 myelinated neurites[46], and we used this quantity in deriving our Nissl-HA measure (see **Methods**).

295 Pyramidal cells constitute 70-80% of cells in the cortex[47]. Due to their shape, pyramidal cell body
296 orientations are reflected in the ST anisotropy measure (**SI Figure 14**). The orientations of apical
297 dendrites are strongly associated with the orientation of pyramidal cell bodies[53], and these non-
298 myelinated neurites are prominent structural features of gray matter which likely influence local
299 diffusion[22,36,38,52]. The arrangement of smaller neural cell bodies into minicolumns along apical dendrite
300 bundles is reflected locally in each cortical layer by our structure tensor methods[22,36–38,52]. It is likely that
301 other accompanying tissue features, such as unmyelinated axons, glial processes, epithelial cells and
302 microvasculature play a role in shaping the correspondence between Nissl-HA and dMRI-FA, and these
303 may all be indicated by patterns in cell body orientations.

304 Nissl-HA may also partly reflect a subset of vertically oriented myelinated axons[22,38,46] in addition to
305 non-myelinated tissue components. The Nissl derived "neuropil fraction"[46] includes some myelinated
306 axons, especially in deep layers[21,22,36–38,46,52]. We observed a median correlation of 0.6 between Nissl-HA
307 and myelin-HA (**SI Figure 6**). However, non-myelinated substructures are more plentiful in gray matter
308 than myelinated[21,22,28,36–38,52]. The lower average correlation (**Figure 4**) and clear differences in the
309 locations of peak anisotropy in the laminar profiles of myelin-HA and dMRI-FA (**Figure 5**, **SI Figure 9**)
310 suggest that myelin is not the primary driver of dMRI-FA or of Nissl-HA, even in deep layers where
311 myelin is very dense.

312 The specific combination of tissue features that shape cortical dMRI-FA cannot be fully known at
313 this point, and thus warrants further investigation. The strong spatial covariation (median 0.76) of Nissl-
314 HA to dMRI-FA holds promise that the structural basis of diffusion MRI in the cortex can be well
315 understood. Future research using more specific stains will be able to assess more details of the relevant
316 structural features, for example using immunohistochemical stains for proteins such as MAP 2[36,37], MAP
317 τ[54], SMI-312[55], SMI-311[55], MBP[56] and GFAP[57] which are variously specific to dendrites, neurites, axons,
318 myelin and glial processes.

319 Previous work has shown that when a white matter voxel is organized as a single bundle[58], myelination
320 and axon integrity are associated with radial and axial diffusivity, respectively[12,13,18]. The present results
321 of Nissl-HA and myelin-HA in the gray matter indicate that myelinated and unmyelinated neurites affect
322 these two components of anisotropy in different ways, consistent with recent theoretical work[11] (**Figure**
323 **6, SI Figure 11**). Such information might potentially be used in biophysically motivated tissue models of
324 the diffusion signal[11,59,60]. In dMRI models of white matter, it is sometimes assumed that intra-neurite
325 axial diffusivity – i.e. the intrinsic rate of diffusion in the axoplasm parallel to the membrane - is
326 constant[60,61]. However, in the more biologically heterogenous environment of gray matter, this
327 assumption may not hold[11]. It may be that the cytoplasm of cell bodies, axons, dendrites and glial
328 processes each have slightly different, characteristic intrinsic diffusivities[30]. The differing anatomy of
329 particular tissue features may also hinder diffusion in specific ways, for example diffusivity in cell bodies
330 may be low due to the high lipid content of cell organelles[62]. Recent modelling efforts in white matter
331 have sought to simultaneously measure both variation in intra-axonal diffusivity, and variation in axon
332 orientation dispersion[60]. Related models may prove especially important in gray matter. Models that
333 include information about myelin levels, cortical curvature and location in the cortical depth, as well as
334 different diffusion times, we may be able to gather very detailed information about the human cortex
335 in-vivo.

336 In order to develop such models, our understanding of the diffusion signal in gray matter should be
337 grounded in strong empirical data. In the present study, we see significant variations in the laminar
338 profiles of dMRI-FA between gray matter regions (**SI Figure 8, SI Figure 9**). This variation may reflect
339 valuable information such as cytoarchitectural differences between cortical regions, or degradation of
340 tissue due to disease. The factors influencing the diffusion signal are likely to differ in different
341 horizontal locations and at different cortical depths. Measurements taken in-vivo at low resolution will
342 represent the influences not only of cyto and myeloarchitecture, but also of cortical curvature[42]. Work at
343 high resolution in ex-vivo animal models is important in order to understand the more ambiguous
344 signals from the more complex human brain at lower resolution. The ex-vivo marmoset model has
345 considerable advantages for this endeavor. As a primate, the marmoset's cortical thickness and
346 cytoarchitectural complexity is comparable to the human case, but its small size means many cortical
347 regions with diverse properties are available at high resolution and with minimal folding confounds. The

348 larger, more complex and folded rhesus brain may form an intermediate subject at somewhat lower
349 spatial resolution, before tackling the much more complex human case at low resolution in-vivo.

350 Diseases such as Alzheimer's are believed to involve subtle changes to tissue properties especially
351 in their early stages, and the ability to gather specific cytoarchitectural information separately from
352 myeloarchitectural in-vivo may be crucial[9], particularly since relatively little post-mortem information is
353 available regarding the early tissue changes. The early stages of Alzheimer's and other diseases of the
354 gray matter neuropil can manifest as cellular damage and inflammation rather than demyelination[63].
355 Changes in mean diffusivity in gray matter have been associated with Alzheimer's pathology[64]. The
356 present findings may inform the development of dMRI models of the gray matter, perhaps to specifically
357 target neuroinflammation[9] or other aspects of Alzheimer's pathology in the earliest stages[65].

358 Our findings may also be useful in the growing field of comparative anatomy[66–70]. MRI methods
359 lack the spatial precision and biochemical specificity of histology. However, the whole brain can be
360 studied at once, non-destructively and in three dimensions. This permits sophisticated computational
361 analysis of the geometric and topological layout of the brain[66], of the spatial trajectories of white matter
362 pathways[67] and of how these may be related between species[68,70]. At present however, analysis of the
363 gray matter structural properties in such studies tends to be limited to myelin levels[66]. The present
364 results may add important information that may help explain differing cognitive abilities between
365 species. For example, the fraction of cortical tissue occupied by neurites differs between humans and
366 chimpanzees[46]. Using dMRI measures of cortical gray matter, we might model not only the quantity, but
367 organization of specifically non-myelinated neurites in gray matter, which may be a marker for the
368 intrinsic connectional sophistication of local gray matter regions. We may be able to compare these
369 tissue properties across whole brains and in many species, in a quantitative way that can be linked to
370 patterns of long-range connectivity via white matter bundles. Such studies might shed light on cortical
371 evolution, the relationships between cortical regions, disease states, the interpretation of the BOLD
372 signal and differing cognitive capabilities between species.

373 Methods

374 We describe below the methods used in this study, sample preparation and MRI acquisition,
375 sectioning and staining, registration and finally statistical analysis.

376 *Animals and materials*

377 The brain of one adult marmoset (female, 5-year-old, "Case P") was used in this study.

378 *Ex vivo high-resolution MRI Acquisition*

379 Before MRI scanning, the formalin-fixed marmoset brain was soaked with 0.15% gadopentetate
380 dimeglumine (Magnevist, Bayer Leverkusen, Germany) for 3 weeks to reduce the T1 relaxation time. In
381 order to improve SNR, brain P was cut through the midline, and each hemisphere was scanned
382 separately with a 25-mm birdcage volume coil.

383 For the left hemisphere Diffusion MRI was collected with a 3D diffusion-weighted spin-echo EPI
384 sequence with a spatial resolution of 150μm isotropic voxel size. The 3D diffusion EPI sequence
385 parameters were: TR = 400 ms, TE = 28.4 ms, flip angle = 90°, FOV = 38.4 x 24 x 21 mm, matrix size = 256
386 x 160 x 140, resolution = 0.15 mm isotropic. Sixty two DWI volumes (2 at b=0, and 60 directions with
387 b=4800) were acquired using 3 averages. The same 62 volumes were collected a second time with
388 identical settings. The total DWI acquisition time was about 58 hours. The pulse width for the diffusion
389 weighting gradient is 6.4 ms and pulse separation is 14 ms.

390

391 The right hemisphere was scanned with 100μm resolution with the 25 mm coil. The parameters for the
392 3D diffusion-weighted spin-echo EPI sequence were: TR = 400 ms, TE = 35 ms, flip angle = 90°, FOV =
393 38.4 x 20 x 25 mm, matrix size = 348 x 200 x 250, resolution = 0.10 mm isotropic, a total of 132 DWI
394 images (6 at b=0, and 126 directions with b = 4800), and total acquisition time was about 55 hours.

395 The left and right hemispheres separately underwent scanning for MTR at 75μm and 150μm
396 respectively.

397 The MTR images were collected with a 3D FLASH sequence. For the resolution of 150μm, the
398 parameters were: TR = 21.5 ms, TE = 3.6 ms, flip angle = 20^0, FOV = 38.4 x 24 x 21 mm, matrix size = 256
399 x 160 x 140, number of averages = 8 and number of repetitions = 6, total acquisition time about 13 hour
400 For the resolution of 75μm acquisition, the parameters are: TR = 21.9 ms, TE = 3.8 ms, flip angle = 20^0,
401 FOV = 34.8 x 20.4 x 20.1 mm, matrix size = 464 x 272 x 268, number of averages=5 and number of

402 repetition = 14, total acquisition time about 60 hours. The magnetization transfer was achieved (in M_{sat}
403 scans} by a Gaussian shaped pulse at either +2000 or -2000 Hz offset frequency; the duration of pulse is
404 12.5 ms and flip angle is 540^0 and the pulse is present in every TR. This magnetization transfer pulse is
405 turned off in M_{off} scans. The MTR value is calculated as $100*(1-M_{sat}/M_{off})$.

406 *MRI Processing*

407 *Diffusion Tensor Estimation* dMRI data was preprocessed using TORTOISE v3[71] which includes code
408 for denoising[72]. After rotation to the histology slice plane (see *Registration of histology and MRI data*
409 below), the diffusion tensor was estimated using FSL 5.0.11 DTIFIT. AD, RD and the in-plane anisotropy[40]
410 were calculated using FSL 5.0.11 fslmaths.

411 Registered dMRI tensor parameter maps and MT data were split into separate coronal 32 bit
412 quantitative tif images and grouped according to slice number for registration.

413 *Histological Processing*

414 *Sectioning and Staining* Following scanning, the brain's left hemisphere was coronally sectioned at
415 50μm on a freezing microtome, while the right hemisphere was sectioned sagittally. Alternate sections
416 were stained for Nissl bodies and for myelin. The Gallyas silver stain for myelin was selected to stain
417 individual axons in high detail[73]. We used the Thionin stain for Nissl bodies. This is a traditional staining
418 method that identifies cell bodies and some dendrites proximal to the soma, but very few axons[53]. Each
419 histological section was scanned at 0.88μm resolution (10x magnification) using a Ziess Axioscan
420 microscope slide scanner. Higher resolution 0.44μm microscopy was not shown to produce significantly
421 different ST results using this data. Histological sections were excluded due to damage or poor stain
422 properties.

423 *Registration of histology and MRI data*

424 *Rigid body rotation to histology slice plane.* For histology to MRI registration, we first performed an
425 initial rigid body alignment of the 75μm MT_sat data (**SI Figure 1**) to match the histology slice plane for
426 each of P's hemispheres. This transformation was estimated by-eye using the mango MRI
427 editor/viewer[74] and the manually transformed MT volume was used as the target for FSL 5.0.11 FLIRT[75]
428 to transform the remainder of the MRI data.

429 *Registration of MT and dMRI.* The 150μm dMRI was rigid body registered to the 75μm MT volume
430 using FSL FLIRT, so that the dMRI was upsampled to 75μm using spline interpolation. The b-vectors were
431 rotated using the FAST transform and custom MATLAB code.

432 *MIND nonlinear registration of local histology ROI*. After performing ST computations on the
433 histology to produce ST anisotropy parameter maps (see *Structure Tensor Analysis of Histological*
434 *Orientations and Anisotropy* below), we performed careful non-linear alignment of nine local frontal and
435 parietal ROI from the histology to the MRI (**SI figure 1**). 75μm resolution stain intensity maps of nine
436 coronal sections of each of Nissl and myelin histology were first binarized using a threshold adjustment
437 in imageJ[76] and then registered to their corresponding MRI slices to correct for histology shrinkage and
438 deformation, first using manual 2D alignment in imageJ[76] and then MIND MATLAB code[77] (α=0.1). To
439 avoid registration between MRI and histological features whose anatomical meanings and relationships
440 were unknown, the registration source and target images were featureless masks of the GM derived
441 from the MT data (**SI figure 1**). Custom MATLAB code was written to store and apply these transforms to
442 ST maps (see *Structure Tensor Analysis of Histological Orientations and Anisotropy* below) and other
443 parameter maps derived from the histology. We selected regions of frontal and parietal cortex for non-
444 linear alignment whose minimal gyrification ensured that the diffusion MRI signal was largely unaffected
445 by cortical curvature[42]. This registration process allowed us to directly compare the cortical variation of
446 diffusion and histological parameters from the same brain.

447 *Structure Tensor Analysis of Histological Orientations and Anisotropy*

448 To estimate the anisotropy and orientation content of the histology we employed the structure
449 tensor method[40]. The 0.88μm per pixel resolution histology images were processed using the structure
450 tensor as implemented in the "OrientationJ" ImageJ package[45], using a local gaussian window of σ=80
451 pixels and image gradients computed with a cubic spline. This was applied to the color channel of the
452 histology that exhibited the strongest image intensity gradients. This was the red channel for Nissl data,
453 or blue channel for Gallyas myelin data. Orientation and anisotropy information were obtained from
454 these data according to

455 $$S_0[p] = \begin{bmatrix} I_x[p]I_x[p] & I_x[p]I_y[p] \\ I_x[p]I_y[p] & I_y[p]I_y[p] \end{bmatrix}$$

456 ***Equation 1****. Pixelwise structure tensor*

where S_0 is the structure tensor at pixel p and Ix, Iy are the partial derivatives of the 2D image intensities at pixel p. Since the dMRI data contains diffusion information gathered over a 150μm cubic area, the histology structure tensor at each pixel was a distance weighted function S_w[p] of the structure tensors S_0 within a radius of 75μm. This was achieved for pixel p by multiplying with gaussian window with a sum of 1, with sigma 85 pixels (75μm), shown in **Equation 2.** The ST angle is shown in **Equation 3** and anisotropy in **Equation 4**

$$S_w[p] = \sum_r w[r] S_0[p-r]$$

Equation 2. *Weighted structure tensor*

$$\theta[p] = \frac{1}{2} arctan\left(2\frac{I_x[p]I_y[p]}{I_y[p]I_y[p] - I_x[p]I_x[p]}\right)$$

Equation 3. *ST orientation*

$$SAnisotropy = \frac{\lambda_1 - \lambda_2}{\lambda_1 + \lambda_2}$$

Equation 4. *Structure tensor anisotropy*

A pipeline was implemented in bash and ImageJ macro language to process the Zeiss axioscan histology output files in CZI format into 32 bit tif format with resolution 0.88μm, and process these with orientationJ. The histology stain intensity data and ST data at 0.88μm were then down sampled into maps of 75μm tiles for comparison and registration to MRI data using MATLAB R2018a. The mean ST angle within 75μm was the circular mean of the 0.88μm angles within that area.

Histological Anisotropy Because diffusion anisotropy is sensitive to both the density and coherence of tissue features, but ST coherence is sensitive only to the latter, we defined composite measures of histological anisotropy. **Myelin-HA** was defined as the product of myelin stain intensity and the ST coherence of the myelin data.

481 For the Nissl-HA we defined the neurite fraction (NF) as 1-nissl intensity, where 1 was defined as
482 the highest gray matter value and 0 was defined as black. Nissl-HA was defined as the product of NF and
483 the ST coherence of the Nissl data.

484 *2D dMRI and Histology ST Tractography*

485 The ST analysis of the myelin and Nissl histology yielded 2D vector fields at 75μm resolution representing
486 the mean 0.88μm ST angle within a tile. For comparison, we projected the 3D dMRI principle eigenvector
487 at the same spatial resolution onto the 2D plane (**Figure 2**).
488
489 The vector fields of the 75μm weighted structure tensor permitted tractography based on histological
490 image properties within areas equivalent to the MRI voxels. We ran identical tractography through the
491 Nissl and myelin ST vector fields. We used a MATLAB package "even streamlines" v 1.1.0.0 to ensure the
492 streamlines were evenly spaced in the horizontal direction[78], modified to use a fixed integration step of
493 0.1 . **SI figure 3** shows tractography through the 2D projected components of the first eigenvector of the
494 diffusion tensor, overlaid on high resolution histology images. We note all three modalities yield very
495 similar results.

496 *Cortical Parcellation and Statistical Analysis*

497 To sample the gray matter for analysis, we took advantage of the fact that cortex consists of vertically
498 oriented tissue components[21,33,36,39] to develop a matrix representation whose columns were derived from
499 data sampled along the vertical dMRI tractography streamlines (**SI Figure 4a**) (see *2D dMRI and Histology*
500 *ST Tractography* above), and whose rows spanned the horizontal direction. We first masked the registered
501 gray matter ROI by thresholding the MT image (M_{sat}), and eroding this mask by 2 75μm pixels to avoid the
502 regions where the diffusion tensor orientations were known not to be vertical (see **Figure 2**). We then ran
503 tractography through the 2d projected principle eigenvectors of the diffusion tensor in the masked region.
504 This produced a set of vertical, non-intersecting streamlines (**SI Figure 4a)** which were numbered from in
505 the horizontal direction.

506 For each histology and MRI parameter map, we sampled a vector of unique pixels whose coordinates
507 intersected one streamline's coordinates. We then resampled each resulting vector of pixels to a fixed

length using bilinear interpolation, to yield a simple matrix representation of the gray matter (**SI Figure 4a**). This operation was invertible such that data in matrix form could be displayed in image space (**SI Figure 4b**).

Our statistical analysis proceeded by parcellating the matrix representation of the non-linearly registered histology and MRI data. We used parcellation in our analysis partly to separate out regions of potentially differing stain intensity, and partly because different anatomical regions of cortex have different constituent myelo- and cytoarchitectural elements[21,37] and may therefore exhibit different relationships between histology and dMRI. For each parcel we took the Pearson correlation between sample variables. Examples are shown in **Figure 3**. **SI Figure 4b** shows parcels of matrix columns of different sizes, represented in image space and colored by the correlation coefficient of histology ST anisotropy to dMRI-FA.

Figure 4 and **Figure 6** show the distribution of correlation coefficients using a parcel size of 5 streamlines which is roughly 300μm in horizontal width. **SI Figure 5** shows that the correlation results are stable for different parcel sizes. For **figure 5** we concatenated matrices from all sections and displayed the mean of all rows. **SI figure 9** shows the mean of rows in each individual section.

References

1. Aggarwal, M., Nauen, D. W., Troncoso, J. C. & Mori, S. Probing region-specific microstructure of human cortical areas using high angular and spatial resolution diffusion MRI. *Neuroimage* **105**, 198–207 (2015).
2. Assaf, Y. Imaging laminar structures in the gray matter with diffusion MRI. *Neuroimage* **197**, 677–688 (2019).
3. Leuze, C. W. U. *et al.* Layer-specific intracortical connectivity revealed with diffusion MRI. *Cereb. Cortex* **24**, 328–339 (2014).
4. Truong, T.-K., Guidon, A. & Song, A. W. Cortical Depth Dependence of the Diffusion Anisotropy in the Human Cortical Gray Matter In Vivo. *PLoS One* **9**, e91424 (2014).
5. Kleinnijenhuis, M. *et al.* Layer-specific diffusion weighted imaging in human primary visual cortex in vitro. *Cortex* **49**, 2569–2582 (2013).

537 6. Jespersen, S. N., Leigland, L. A., Cornea, A. & Kroenke, C. D. Determination of Axonal and Dendritic
538 Orientation Distributions Within the Developing Cerebral Cortex by Diffusion Tensor Imaging. *IEEE*
539 *Trans. Med. Imaging* **31**, 16–32 (2012).

540 7. Jespersen, S. N. *et al.* Neurite density from magnetic resonance diffusion measurements at
541 ultrahigh field: Comparison with light microscopy and electron microscopy. *Neuroimage* **49**, 205–
542 216 (2010).

543 8. Brodmann, K. *Vergleichende lokalisationslehre der großhirnrinde in ihren prinzipien dargestellt auf*
544 *grund des zellenbaues (1909)(English translation available in Garey, L.J. (2006). Brodmann's:*
545 *Localisation in the cerebral cortex. 3rd Edition. Springer US)*. (Springer US, 2006).

546 9. Weston, P. S. J., Simpson, I. J. A., Ryan, N. S., Ourselin, S. & Fox, N. C. Diffusion imaging changes in
547 grey matter in Alzheimer's disease: A potential marker of early neurodegeneration. *Alzheimer's*
548 *Res. Ther.* **7**, 1–8 (2015).

549 10. O'Doherty, D. C. M., Chitty, K. M., Saddiqui, S., Bennett, M. R. & Lagopoulos, J. A systematic review
550 and meta-analysis of magnetic resonance imaging measurement of structural volumes in
551 posttraumatic stress disorder. *Psychiatry Res. - Neuroimaging* **232**, 1–33 (2015).

552 11. Lampinen, B. *et al.* Searching for the neurite density with diffusion MRI: Challenges for biophysical
553 modeling. *Hum. Brain Mapp.* **40**, 2529–2545 (2019).

554 12. Mancini, M. *et al.* An interactive meta-analysis of MRI biomarkers of Myelin. *Elife* **9**, 1–23 (2020).

555 13. Lazari, A. & Lipp, I. Can MRI measure myelin? Systematic review, qualitative assessment, and meta-
556 analysis of studies validating microstructural imaging with myelin histology. *Neuroimage* **230**,
557 117744 (2021).

558 14. Calamante, F., Jeurissen, B., Smith, R. E., Tournier, J. D. & Connelly, A. The role of whole-brain
559 diffusion MRI as a tool for studying human in vivo cortical segregation based on a measure of
560 neurite density. *Magn. Reson. Med.* **79**, 2738–2744 (2018).

561 15. Fukutomi, H. *et al.* Neurite imaging reveals microstructural variations in human cerebral cortical
562 gray matter. *Neuroimage* **182**, 1–12 (2018).

563 16. Roosendaal, S. D. *et al.* Regional DTI differences in multiple sclerosis patients. *Neuroimage* **44**,
564 1397–1403 (2009).

565 17. Song, S. K. *et al.* Diffusion tensor imaging detects and differentiates axon and myelin degeneration
566 in mouse optic nerve after retinal ischemia. *Neuroimage* **20**, 1714–1722 (2003).

567 18. Song, S. K. *et al.* Dysmyelination revealed through MRI as increased radial (but unchanged axial)
568 diffusion of water. *Neuroimage* **17**, 1429–1436 (2002).

569 19. Song, S. K. *et al.* Demyelination increases radial diffusivity in corpus callosum of mouse brain.
570 *Neuroimage* **26**, 132–140 (2005).

571 20. Stricker, N. H. *et al.* Decreased white matter integrity in late-myelinating fiber pathways in
572 Alzheimer's disease supports retrogenesis. *Neuroimage* **45**, 10–16 (2009).

573 21. Peters, A. & Sethares, C. Myelinated axons and the pyramidal cell modules in monkey primary
574 visual cortex. *J. Comp. Neurol.* **365**, 232–255 (1996).

575 22. Buxhoeveden, D. P. & Casanova, M. F. The minicolumn hypothesis in neuroscience. *Brain* **125**, 935–

576 951 (2002).

577 23. Lewis, J. W. & Van Essen, D. C. Mapping of architectonic subdivisions in the macaque monkey, with
578 emphasis on parieto-occipital cortex. *J. Comp. Neurol.* **428**, 79–111 (2000).

579 24. Van der Weijden, C. W. J. *et al.* Myelin quantification with MRI: A systematic review of accuracy
580 and reproducibility. *Neuroimage* **226**, 117561 (2020).

581 25. Glasser, M. F. & Van Essen, D. C. Mapping human cortical areas in vivo based on myelin content as
582 revealed by T1- and T2-weighted MRI. *J. Neurosci.* **31**, 11597–11616 (2011).

583 26. Kleinnijenhuis, M. *et al.* Detailed laminar characteristics of the human neocortex revealed by
584 NODDI and histology. *Organ. Hum. Brain Mapp.* 3815 (2013).

585 27. Vogt, C. & Vogt, O. Allgemeinere Ergebnisse unserer Hirnforschung. *J Psychol Neurol* **25**, 279–461
586 (1919).

587 28. Schüz, A., Braitenberg, V. & Miller, S. R. The Human Cortical White Matter: Quantitative Aspects of
588 Cortico-Cortical Long-Range Connectivity. in *Cortical Areas* 377–385 (CRC Press, 2002).

589 29. Wang, Y., Ye, M., Kuang, X., Li, Y. & Hu, S. A simplified morphological classification scheme for
590 pyramidal cells in six layers of primary somatosensory cortex of juvenile rats. *IBRO Reports* **5**, 74–
591 90 (2018).

592 30. Beaulieu, C. The basis of anisotropic water diffusion in the nervous system - A technical review.
593 *NMR Biomed.* **15**, 435–455 (2002).

594 31. Jones, D. K., Knösche, T. R. & Turner, R. White matter integrity, fiber count, and other fallacies: The
595 do's and don'ts of diffusion MRI. *Neuroimage* **73**, 239–254 (2013).

596 32. Jespersen, S. N., Kroenke, C. D., Østergaard, L., Ackerman, J. J. H. & Yablonskiy, D. A. Modeling
597 dendrite density from magnetic resonance diffusion measurements. *Neuroimage* **34**, 1473–1486
598 (2007).

599 33. Reveley, C. *et al.* Superficial white matter fiber systems impede detection of long-range cortical
600 connections in diffusion MR tractography. *Proc. Natl. Acad. Sci.* **112**, E2820–E2828 (2015).

601 34. Miller, K. L. *et al.* Diffusion imaging of whole, post-mortem human brains on a clinical MRI scanner.
602 *Neuroimage* **57**, 167–181 (2011).

603 35. McNab, J. A. *et al.* High resolution diffusion-weighted imaging in fixed human brain using diffusion-
604 weighted steady state free precession. *Neuroimage* **46**, 775–785 (2009).

605 36. Rockland, K. S. & Ichinohe, N. Some thoughts on cortical minicolumns. *Exp. Brain Res.* **158**, 265–
606 277 (2004).

607 37. Peters, A., Manuel Cifuentes, J. & Sethares, C. The organization of pyramidal cells in area 18 of the
608 rhesus monkey. *Cereb. Cortex* **7**, 405–421 (1997).

609 38. Buxhoeveden, D. P. & Casanova, M. F. The minicolumn and evolution of the brain. *Brain. Behav.*
610 *Evol.* **60**, 125–151 (2002).

611 39. Pierpaoli, C., Jezzard, P., Basser, P. J., Barnett, A. & Di Chiro, G. Diffusion tensor MR imaging of the
612 human brain. *Radiology* **201**, 637–648 (1996).

613 40. Budde, M. D. & Frank, J. A. Examining brain microstructure using structure tensor analysis of

614 histological sections. *Neuroimage* **63**, 1–10 (2012).

615 41. Heath, F., Hurley, S. A., Johansen-Berg, H. & Sampaio-Baptista, C. Advances in noninvasive myelin
616 imaging. *Dev. Neurobiol.* **78**, 136–151 (2018).

617 42. Kleinnijenhuis, M. *et al.* Diffusion tensor characteristics of gyrencephaly using high resolution
618 diffusion MRI in vivo at 7T. *Neuroimage* **109**, 378–387 (2015).

619 43. Bock, N. A., Hashim, E., Kocharyan, A. & Silva, A. C. Visualizing myeloarchitecture with magnetic
620 resonance imaging in primates. *Ann. N. Y. Acad. Sci.* **1225**, E171–E181 (2011).

621 44. Liu, C. *et al.* Marmoset Brain Mapping V3: Population multi-modal standard volumetric and
622 surface-based templates. *Neuroimage* **226**, 117620 (2021).

623 45. Püspöki, Z., Storath, M., Sage, D. & Unser, M. Transforms and operators for directional bioimage
624 analysis: A survey. *Adv. Anat. Embryol. Cell Biol.* **219**, 69–93 (2016).

625 46. Spocter, M. A. *et al.* Neuropil distribution in the cerebral cortex differs between humans and
626 chimpanzees. *J. Comp. Neurol.* **520**, 2917–2929 (2012).

627 47. Jones, E. G. Laminar distribution of cortical efferent cells. *Cereb. cortex* 521–552 (1984).

628 48. Lübke, J., Egger, V., Sakmann, B. & Feldmeyer, D. Columnar organization of dendrites and axons of
629 single and synaptically coupled excitatory spiny neurons in layer 4 of the rat barrel cortex. *J.*
630 *Neurosci.* **20**, 5300–5311 (2000).

631 49. Oberlaender, M. *et al.* Cell type-specific three-dimensional structure of thalamocortical circuits in
632 a column of rat vibrissal cortex. *Cereb. Cortex* **22**, 2375–2391 (2012).

633 50. Basser, P. J., Mattiello, J. & LeBihan, D. MR diffusion tensor spectroscopy and imaging. *Biophys. J.*
634 **66**, 259–267 (1994).

635 51. Buldyrev, S. V. *et al.* Description of microcolumnar ensembles in association cortex and their
636 disruption in Alzheimer and Lewy body dementias. *Proc. Natl. Acad. Sci. U. S. A.* **97**, 5039–5043
637 (2000).

638 52. Jones, E. G. Microcolumns in the cerebral cortex. *Proc. Natl. Acad. Sci. U. S. A.* **97**, 5019–5021
639 (2000).

640 53. Windle, W. F., Rhines, R. & Rankin, J. A Nissl Method Using Buffered Solutions of Thionin. *Stain*
641 *Technol.* **18**, 77–86 (1943).

642 54. Kosik, K. S., Joachim, C. L. & Selkoe, D. J. Microtubule-associated protein tau (τ) is a major antigenic
643 component of paired helical filaments in Alzheimer disease. *Proc. Natl. Acad. Sci. U. S. A.* **83**, 4044–
644 4048 (1986).

645 55. Ulfig, N., Nickel, J. & Bohl, J. Monoclonal antibodies SMI 311 and SMI 312 as tools to investigate
646 the maturation of nerve cells and axonal patterns in human fetal brain. *Cell Tissue Res.* **291**, 433–
647 443 (1998).

648 56. Deibler, G. E., Martenson, R. E. & Kies, M. W. Large Scale Preparation of Myelin Basic Protein from
649 Central Nervous Tissue of Several Mammalian Species. *Prep. Biochem.* **2**, 139–165 (1972).

650 57. Eng, L. F. & Ghirnikar, R. S. GFAP and Astrogliosis. *Brain Pathol.* **4**, 229–237 (1994).

651 58. Wheeler-Kingshott, C. A. M. & Cercignani, M. About 'axial' and 'radial' diffusivities. *Magn. Reson.*

652 *Med.* **61**, 1255–1260 (2009).

653 59. Novikov, D. S., Fieremans, E., Jespersen, S. N. & Kiselev, V. G. Quantifying brain microstructure with
654 diffusion MRI: Theory and parameter estimation. *NMR Biomed.* **32**, 1–53 (2019).

655 60. Howard, A. F. D. *et al.* Estimating intra-axonal axial diffusivity with diffusion MRI in the presence of
656 fibre orientation dispersion. *bioRxiv* 1–33 (2020).

657 61. Zhang, H., Schneider, T., Wheeler-Kingshott, C. A. & Alexander, D. C. NODDI: Practical in vivo
658 neurite orientation dispersion and density imaging of the human brain. *Neuroimage* **61**, 1000–
659 1016 (2012).

660 62. Morré, D. J. & Mollenhauer, H. H. endomembrane concept: a functional integration of endoplasmic
661 reticulum and Golgi apparatus. *Dyn. Asp. Plant Ultrastruct. AW Robards, ed* (1974).

662 63. Wenk, G. L. Neuropathologic changes in Alzheimer's disease. *J. Clin. Psychiatry* **64**, 7–10 (2003).

663 64. Montal, V. *et al.* Cortical microstructural changes along the Alzheimer's disease continuum.
664 *Alzheimer's Dement.* **14**, 340–351 (2018).

665 65. Sato, K. *et al.* A non-human primate model of familial Alzheimer's disease. *bioRxiv*
666 2020.08.24.264259 (2020).

667 66. Eichert, N. *et al.* Cross-species cortical alignment identifies different types of anatomical
668 reorganization in the primate temporal lobe. *Elife* **9**, 1–30 (2020).

669 67. Roumazeilles, L. *et al. Longitudinal connections and the organization of the temporal cortex in*
670 *macaques, great apes, and humans*. *PLoS biology* **18**, (2020).

671 68. Mars, R. B. *et al.* Whole brain comparative anatomy using connectivity blueprints. *Elife* **7**, 1–15
672 (2018).

673 69. Mars, R. B. *et al.* Primate comparative neuroscience using magnetic resonance imaging: promises
674 and challenges. *Front. Neurosci.* **8**, 298 (2014).

675 70. Xu, T. *et al.* Cross-species functional alignment reveals evolutionary hierarchy within the
676 connectome. *Neuroimage* **223**, 117346 (2020).

677 71. Irfanoglu, M. O., Nayak, A., Jenkins, J. & Pierpaoli, C. TORTOISE v3 : Improvements and New
678 Features of the NIH Diffusion MRI Processing Pipeline. in *ISMRM 25th annual meeting* 9–11 (2018).

679 72. Veraart, J. *et al.* Denoising of diffusion MRI using random matrix theory. *Neuroimage* **142**, 394–
680 406 (2016).

681 73. Gallyas, F. Silver staining of myelin by means of physical development. *Neurol. Res.* **1**, 203–209
682 (1979).

683 74. Lancaster, J. L. *et al.* Automated regional behavioral analysis for human brain images. *Front.*
684 *Neuroinform.* **6**, 1–12 (2012).

685 75. Jenkinson, M., Bannister, P., Brady, M. & Smith, S. Improved Optimization for the Robust and
686 Accurate Linear Registration and Motion Correction of Brain Images. *Neuroimage* **17**, 825–841
687 (2002).

688 76. Schindelin, J. *et al.* Fiji: An open-source platform for biological-image analysis. *Nat. Methods* **9**,
689 676–682 (2012).

77. Heinrich, M. P. *et al.* MIND: Modality independent neighbourhood descriptor for multi-modal deformable registration. *Med. Image Anal.* **16**, 1423–1435 (2012).

78. Jobard, B. & Lefer, W. Creating Evenly-Spaced Streamlines of Arbitrary Density. in *Proceedings of the Eurographics Workshop in Boulogne-sur-Mer France* 43–55 (1997).

Acknowledgements

This research was supported by the Intramural Research Program of the National Institute of Mental Health (ZIC MH002899), C.R. and R.B.M. were supported by the Wellcome Centre for Integrative Neuroimaging (Wellcome Trust, 203139/Z/16/Z), and a Biotechnology and Biological Sciences Research Council grant to RBM (BBSRC UK,BB/N019814/1). High resolution MRI data was collected on the 7T Bruker scanner of Dr. Afonso Silva in NINDS. Scanning of brain sections was carried out in the Systems Neuroscience Imaging Resource under Dr. Ted Usdin in NIMH. The authors thank David Yu for histology processing.

Author contributions

C.R. Initiated the study; C.R., F.Q.Y, R.B.M and D.A.L. designed research; F.Q.Y. acquired data; C.R. analysed data; D.A.L. and F.Q.Y. refined the analysis strategy; C.R. wrote the initial manuscript draft; D.A.L., F.Q.Y. and R.B.M. edited the manuscript; All authors discussed results.

Competing Interests

The authors declare no competing interests.

Figure Legends

Figure 1. Comparison of dMRI-FA to corresponding myelin histology and MTR MRI data obtained from the same tissue in the right hemisphere of a marmoset monkey brain. a) Sagittal sections of dMRI-FA (top), Myelin histology (center) and MTR MRI (bottom). The spatial variation of dMRI-FA in vertical (laminar) and horizontal direction showed minimal correspondence with the pattern of myelin intensity, but the variation of the MTR MRI closely mirrored the myelin variation. In some regions of high

715 myelination, the dMRI-FA was high (red arrow) whereas in others it was low (blue arrow). b) Normalized
716 average laminar profiles of FA, MTR and myelin intensity through the cortical thickness in the brain's left
717 hemisphere, derived from cortical parcellation (see **Methods**, **Figure 3**). c) Histogram of correlation
718 coefficients between MRI variables and histological myelin intensity over the nine sections of coronal
719 histology used in this study. MTR MRI shows much higher correspondence with myelin intensity than
720 dMRI-FA does.

721 **Figure 2**. Properties of directional MRI and histology data. For comparison with MRI data, the weighted
722 structure tensor of the myelin and Nissl histology images was computed over a 150μm area (see
723 **Methods**). **a**) Orientation data derived from Nissl and myelin histology and from dMRI are similar,
724 showing columnar, vertically oriented vectors. The overall pattern of orientations in the gray matter is
725 remarkably similar for the data computed from histology and from dMRI. **b**) Diffusion MRI anisotropy
726 and histology-derived anisotropy maps. (see **Methods**).

727 **Figure 3.** Example correlation of Histology and MRI variables sampled in columnar parcels. Top row:
728 non-linearly co-registered histology parameter maps and MRI at 75μm resolution. The red trapezoids
729 indicate a columnar parcel example. Bottom row shows representative scatter plots and Pearson
730 correlation coefficients between histological variables and MRI variables.

731 **Figure 4.** The distribution of correlation coefficients between histological parameters and dMRI-FA over
732 all 393 parcels of cortex. Each point in the distribution is the Pearson correlation between the variables
733 sampled in a vertical parcel (see **Methods**). Red dot shows median value, blue line shows mean and
734 vertical gray bars show lower and upper quartiles. **a)** Correlation of Histological variables to dMRI-FA **b)**
735 Correlation of MTR to myelin intensity.

736 **Figure 5.** Average laminar profiles of FA, Nissl-HA and myelin-HA across all parcels, and the results of a
737 spatial randomization condition to test the regional specificity of parcel-wise histology to MRI
738 correlations. The results show Nissl-HA more closely matches the laminar profile of dMRI-FA, and is
739 more sensitive to shuffling of horizontal MRI locations **a)** Normalized laminar profiles of dMRI-FA,
740 Myelin-HA and Nissl-HA through the cortical thickness, computed from the average of all columnar
741 parcels (see **Methods**). WGB indicates the white/gray matter boundary, PIA indicates the pial surface
742 (see **Methods, Figure 3**) **b)** The change in mean correlation coefficient when the cortical parcels of the

743 histology parameters and those of the dMRI-FA are shuffled between random horizontal locations. Bars
744 indicate standard error. The star indicates significance under a paired t-test.

745 **Figure 6.** Distribution of correlation coefficients between dMRI or histological anisotropy and directional
746 diffusivities. Nissl-HA exhibits a profile that is more similar to dMRI-FA than that of myelin-HA. **a)** dMRI-
747 FA correlates to increases vertical diffusivity (AD) and decreases in horizontal diffusivity (RD). **Top Right**
748 Nissl histological anisotropy (Nissl-HA) exhibits modest positive correlation to AD and negative
749 correlation to RD, indicating that Nissl-HA and dMRI are associated with a similar mechanism of diffusion
750 anisotropy. **Bottom Right** myelin histological anisotropy exhibits no mean correlation to vertical
751 diffusivity and very strong correlation to horizontal diffusivity, as predicted from previous studies [18]

752 **Figure 7.** In granular cortex, layer 4 is identifiable in Nissl histology by many small cell bodies and in
753 myelin histology by a local decrease in stain intensity. In dMRI data layer 4 is associated with a local
754 increase in Axial diffusivity (AD) and in MTR data by a band of low intensity. **a)** dMRI, MTR and
755 histologically derived contrasts. **B) Left** Illustrative detail of the Nissl histology from an ROI of granular
756 cortex. The internal granule layer is visible as a band of small, round cells. **Middle** the same region in
757 myelin histology exhibits a gap in myelination. CLAHE contrast enhancement was applied uniformly
758 across both myelin and Nissl images for display **Right** The highly branched, unmyelinated layer 4
759 terminals of axons from 8 thalamic afferent cells in rat Barrel cortex, reproduced from[49].

760